

∂PV : An End-to-End Differentiable Solar-Cell Simulator

Sean Mann^a, Eric Fadel^a, Samuel S. Schoenholz^b, Ekin D. Cubuk^b, Steven G. Johnson^a, Giuseppe Romano^a

^a*Massachusetts Institute of Technology, 77 Massachusetts Avenue, Cambridge, Massachusetts 02139, USA*

^b*Google Brain, Google Inc., Mountain View, California 94043, USA*

Abstract

We introduce ∂PV , an end-to-end differentiable photovoltaic (PV) cell simulator based on the drift-diffusion model and Beer–Lambert law for optical absorption. ∂PV is programmed in Python using JAX, an automatic differentiation (AD) library for scientific computing. Using AD coupled with the implicit function theorem, ∂PV computes the power conversion efficiency (PCE) of an input PV design as well as the derivative of the PCE with respect to any input parameters, all within comparable time of solving the forward problem. We show an example of perovskite solar-cell optimization and multi-parameter discovery, and compare results with random search and finite differences. The simulator can be integrated with optimization algorithms and neural networks, opening up possibilities for data-efficient optimization and parameter discovery.

Keywords: photovoltaic; energy; drift-diffusion.

PROGRAM SUMMARY

Program Title: ∂PV

CPC Library link to program files: (to be added by Technical Editor)

Developer's repository link: <https://github.com/romanodev/deltapv.git>

Code Ocean capsule: (to be added by Technical Editor)

Licensing provisions: MIT

Programming language: Python

*Corresponding authors.
E-mail address: seanmann@mit.edu, romanog@mit.edu

Nature of problem: Photovoltaic cell optimization has been traditionally difficult due to the lack of gradients from numerical drift-diffusion solvers. This results in the need to treat the problem as a case of black-box optimization, which incurs high computational costs and low data efficiency.

Solution method: An end-to-end differentiable photovoltaic simulator via the drift-diffusion model was developed using JAX, a growing scientific computation and automatic-differentiation library. To enhance computational speed, the implicit function theorem was used to bypass the need for directly differentiating through iterative solvers.

1. Introduction

Numerical modelling of solar cells has become an essential tool of photovoltaic research. A number of packages have been extensively developed, and are freely available, such as PC-1D [1], SCAPS [2], wxAMPS [3] or SESAME [4]. Such simulators have brought significant advances in studying solar cells, and have been applied to common systems including CdS-CdTe [5] and perovskite cells [6]. These computational tools also allow the study of important physical phenomena such as the effects of grain boundaries [7] and defects [8], that impact the performance of solar cells. Although solar cell modelling is quite well developed, the optimization of solar cells is much more challenging, particularly in the case of optimizing many design variables jointly. This is in part due to the unavailability of derivatives, which are key to efficient high-dimensional optimization.

In this work we present ∂PV , a 1D simulation tool for PV cells which solves the drift-diffusion equations using the JAX automatic differentiation (AD) package [9]. ∂PV is able to compute not only the efficiency of the solar cell but also its derivative with respect to any material property set by the user. Thus, this new computational tool enables extensive, efficient materials optimization for PV cells, and can be used in conjunction with standard optimization methods, or machine learning algorithms. By computing derivatives with AD, we avoid numerical and scaling issues associated with the finite-difference technique, while adding complexity comparable to that of the original problem [10]. In passing, we note that, thanks to AD libraries such as JAX [9], Autograd [11] and Zygote [12], several AD-enhanced simulators have been released, including for molecular dynamics [13, 14], fluid dynamics [15], kinetics [16], optics [17] and general purpose solvers [18].

∂PV , therefore, complements the existing offer of AD-based solvers and, relying on the composability of these tools, potentially enables end-to-end differentiability of more advanced multiphysics simulations where the DD model is coupled with full Maxwell equations.

The manuscript is organized as follows. We first provide a brief overview of the drift-diffusion model and its parameters. Second, we detail several technical aspects of the gradient calculations. In the third section, we describe the software architecture and its API. Then, we show an example optimization of a perovskite solar cell. Finally, we use ∂PV for material parameter discovery. ∂PV is a Python package freely distributed under the “MIT” license.

2. Model

Solar cells are commonly modelled by the drift-diffusion (DD) model, a set of coupled nonlinear differential equation describing charge dynamics under illumination. Although this approach suffers from several limitations, the main one being its simplified treatment of band diagrams, it offers a compelling trade-off between accuracy and efficiency. A comprehensive review can be found in Ref. 19. As detailed in Appendix A, the DD model is a nonlinear relationship between the electrostatic potential $\phi(\mathbf{r})$ and the electrochemical potentials for electrons ($\phi_n(\mathbf{r})$) and holes ($\phi_p(\mathbf{r})$), which, after discretization, takes the form

$$\mathbf{f}(\mathbf{u}, \mathbf{p}) = 0; \quad (1)$$

where the unknown $\mathbf{u} = \text{vec}(\phi, \phi_n, \phi_p)$ is a vector of the discretized potentials. The term \mathbf{p} includes M material parameters, the reverse voltage V , and the illumination S (used to calculate the carrier generation density via the Beer–Lambert law; see Appendix B). The boundary conditions for both the equilibrium case (e.g. $S = 0$) and general case are reported in Appendix C. The function f appearing in Eq. 1 represents a set of coupled nonlinear differential equations, and is solved using the Newton–Raphson method: starting from an initial guess, \mathbf{u}^0 , successive steps are the solution of the linear system:

$$\mathbf{f}_\mathbf{u}(\mathbf{u}^{(i)}) \Delta \mathbf{u}^{(i)} = -\mathbf{f}(\mathbf{u}^{(i)}), \quad (2)$$

where $\mathbf{f}_\mathbf{u}^{-1}$ is the Jacobian of \mathbf{f} . Equation 2 is stopped upon convergence, i.e. when $|\Delta \mathbf{u}^{(i)}| < \epsilon$. Note that we use subscripts to refer to partial derivatives,

except when it is clear from the context that it is a vector index. The Newton method displays quadratic convergence only when the trial function is sufficiently close to the root [20], and is not numerically robust when used on its own in practice. Furthermore, the DD model contains exponentials of the potentials, often resulting in convergence stagnation. To mitigate these issues, we employ a modified version of the Newton algorithm, as described in Appendix F. The DD itself is discretized using the Scharfetter–Gummel scheme, which is based on finite differences (for details see Appendix D). Lastly, the linear system in Eq. 2 is solved with the preconditioned generalized minimal residual method (GMRES), which was recently included in JAX. Since this method is *matrix-free*, it allows us to exploit the sparsity of our problem by directly providing the linear operator representing the product of the Jacobian and an arbitrary vector. For these problems, a preconditioner can dramatically speed up convergence; we use an *ILU(0)* preconditioner, as detailed in Appendix E. In order to compute the power conversion efficiency (PCE) of a PV cell, the DD equations must be solved for multiple reverse bias voltages from zero up to the open-circuit voltage V_{oc} where the current through the cell reaches zero. The efficiency is computed as

$$\eta = \frac{P_{\text{MPP}}}{P_{\text{in}}} \quad (3)$$

where P_{in} is the power of the incoming radiation, and P_{MPP} is the maximal power point, i.e. the maximum electrical power $P = I(V) \cdot V$, I being the electrical current. The device optimization, therefore, requires the gradient of the output power with respect to V as well as to the device parameters \mathbf{p} . In the case of maximizing the efficiency of a cell over material parameters, the bias voltage V can be treated simply as an additional optimization variable. For convenience, let us define the vector $\tilde{\mathbf{p}} = [V, \mathbf{p}^\top]^\top$; the gradient of the power output with respect to $\tilde{\mathbf{p}}$ is

$$\frac{dP_{\text{out}}}{d\tilde{\mathbf{p}}} = \frac{d(IV)}{d\tilde{\mathbf{p}}} = V \frac{dI}{d\tilde{\mathbf{p}}} + I \mathbf{e}_1 \quad (4)$$

where \mathbf{e}_1 refers to the unit vector corresponding to the first component of $\tilde{\mathbf{p}}$ (i.e. V). Note that I depends on $\tilde{\mathbf{p}}$ both directly and via the solutions \mathbf{u} :

$$\frac{dI}{d\tilde{\mathbf{p}}} = I_{\mathbf{u}} \mathbf{u}_{\tilde{\mathbf{p}}} + I_{\tilde{\mathbf{p}}}, \quad (5)$$

where we used subscripts to indicate partial derivatives. The terms $I_{\mathbf{u}}$ and $I_{\hat{\mathbf{p}}}$ in Eq. H.2 are readily available using AD; however, differentiating \mathbf{u} with respect to $\hat{\mathbf{p}}$ requires care. Since ∂PV is built in JAX, which supports taking arbitrary gradients and Jacobians of functions, it is technically possible to directly differentiate the PDE solution using AD. In practice, the large number of iterations, including those from the Newton–Raphson method, need to be unrolled and differentiated through the chain rule, which leads to significant computation time and memory usage. Fortunately, there is a simple way to bypass differentiating through the solver: implicitly differentiating the PDE system using the implicit function theorem (IFT) [21, 22]. A brief overview of the IFT applied to our case is given in Appendix G.

3. Software Architecture

3.1. Simulation object

∂PV revolves around the `PVDesign` object, which contains all design parameters of a candidate PV cell. JAX follows a functional programming paradigm to facilitate defining gradients of actions performed on immutable, stateless objects. Hence, ∂PV defines a series of operations on an immutable `PVDesign`, each returning a new object.

We illustrate the usage of ∂PV with a simple example. First, we import necessary packages:

```
import deltapv as dpv
from jax import numpy as jnp, grad
```

Note that we use JAX’s `numpy`, which has virtually the same API as the well-known `numpy` package [23] with the exception of arrays being immutable. In this example, we work with a p–n homojunction. First, we define a custom material as follows:

```
material = dpv.create_material(Chi=3.9,
                               Eg=1.5,
                               eps=9.4,
                               Nc=8e17,
                               Nv=1.8e19,
                               mn=100,
                               mp=100,
```

```
tn=1e-8,
tp=1e-8,
A=2e4)
```

∂PV is also equipped with a rudimentary materials library, including several common semiconductor materials. To load silicon, for example, one could instead use

```
material = dpv.load_material("Si")
```

∂PV has a simple API that, for most purposes, enables defining a `PVDesign` object in one line. To define a p-n junction of thickness 2×10^{-4} cm, where the junction is in the middle, and discretized on 500 uniform grid points, we can use

```
des = dpv.make_design(n_points=500,
                      Ls=[1e-4, 1e-4],
                      mats=material,
                      Ns=[1e17, -1e17],
                      Snl=1e7,
                      Snr=0,
                      Spl=0,
                      Spr=1e7)
```

which creates such a junction with donor density 1×10^{17} cm $^{-3}$ on the left and an equal acceptor density on the right. The surface recombination velocities are as specified, in cm/s.

The simulation can be started with

```
results = dpv.simulate(des)
```

where the equilibrium case is first computed. The solver then applies an increasing reverse bias until V_{oc} is reached. The light source used defaults to the solar spectrum, and can be specified with a `LightSource` object, which is passed into `simulate`, if necessary. The final result, including the PCE and the *IV* curve, is then stored in a dictionary. ∂PV determines the efficiency of this cell to be 19.98%. Several plotting functions are provided, which can be generated via

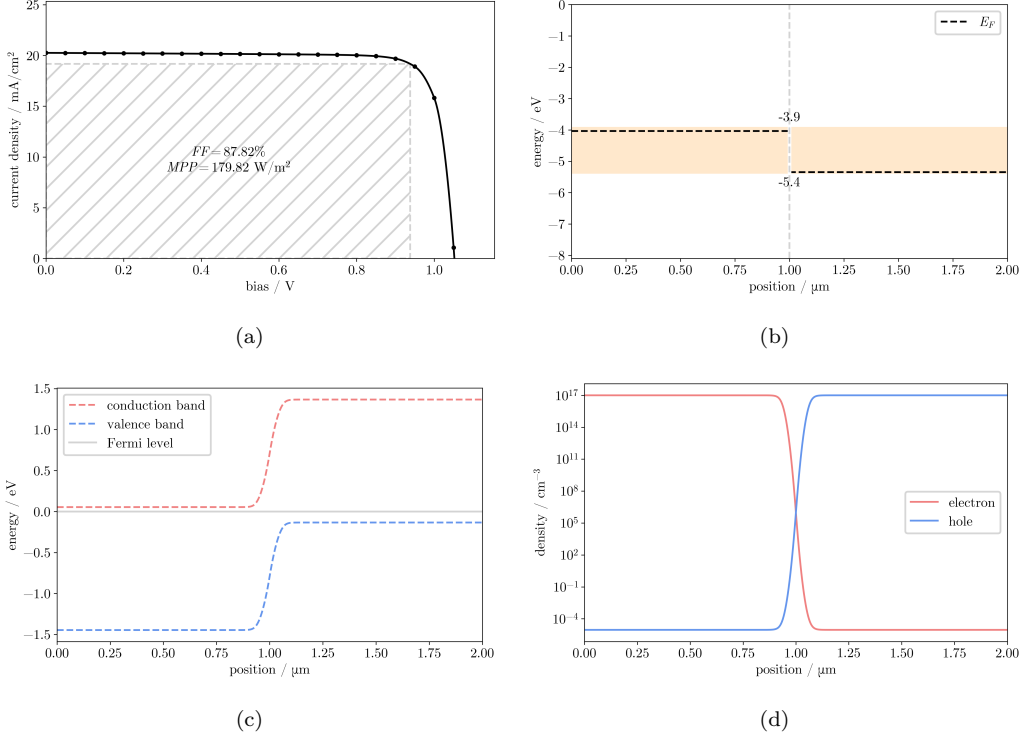


Figure 1: The case of a p-n homojunction. (a) *IV* curve, (b) isolated energy levels, (c) equilibrium band diagram, (d) equilibrium carrier densities.

```
dpv.plot_iv_curve(*results["iv"])
dpv.plot_bars(des)
dpv.plot_band_diagram(des, results["eq"], eq=True)
dpv.plot_charge(des, results["eq"])
```

giving the plots in Figure 1.

The *IV* curve and band diagram for this example have been checked against SESAME [4], with an error within 0.1%. Note that SESAME does not provide an optical model, and thus the generation density $G(x)$ computed by ∂PV was extracted and directly passed into the SESAME simulation.

Taking the gradients is as simple as treating `simulate` as any other differentiable function in JAX's API. To get the partial derivatives of the PCE with respect to all parameters of the `PVDesign`, one could use

```
f = lambda des: dpv.simulate(des)["eff"]
dfddes = grad(f)(des)
```

which gives an object, of the same structure as a `PVDesign`, but where every parameter is replaced with the *derivative* of the PCE with respect to the parameter itself. Due to the availability of AD, the ∂PV simulation procedure can be composed with other calculations and differentiated through directly. This means that a user may define a wrapper function around it with a small number of arguments, and only compute the derivatives with respect to these higher-level, composed parameters. For example, for a single p–n homojunction with uniform material, the problem can be parameterized with a single set of material parameters, with no dependence on x . This may be more useful in many cases when a parameter cannot be continuously varied over space.

4. Examples

4.1. Optimizing a p–i–n Perovskite Solar Cell

In this section we demonstrate several benefits of having a differentiable simulator. The most obvious use case would be gradient-based PCE optimization. Traditionally, solar cell optimization has been done with a variety of gradient-free black box optimization techniques, such as Particle Swarm and Genetic Algorithm [24]. Where the solar cell simulator is treated as a black box without any additional information, optimization becomes a data-intensive task. In particular, it is often intractable to simultaneously optimize more than several parameters in conjunction. Taking brute-force optimization as an example, this challenge is owing to the number of samples required to comprehensively search a set of box-constrained parameters growing exponentially in the number of parameters. Where gradients are available, however, optimization becomes a much easier task, and this becomes starker as the number of parameters grows. An arsenal of well-developed nonlinear optimization algorithms become available with the introduction of analytical gradients.

To illustrate this, we take the case of optimizing a p–i–n perovskite cell, which has been a device attracting much recent interest in the PV community [6]. In particular, we optimize the band gap E_g , electron affinity χ , dielectric constant ϵ , electron and hole densities of states (DOS) N_c, N_v and mobilities m_n, m_p , and dopant densities N_a, N_d for both the electron (ETL) and hole transport layers (HTL). This amounts to 16 parameters. In addition, we employ reasonable box constraints and the following band-alignment

constraints taken from a previous work [24]:

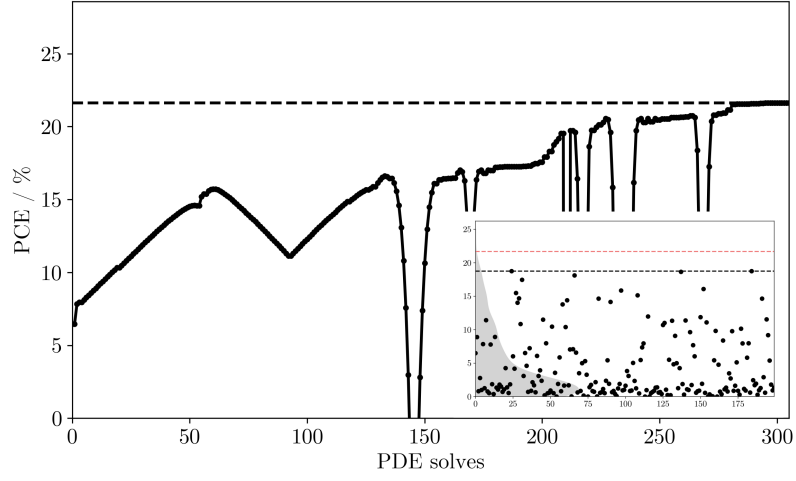
$$\begin{aligned}
\chi_{ETM} - \Phi_F &\leq 0 \\
\chi_{ETM} - \chi_P &\leq 0 \\
\Phi_B - \chi_{HTM} - E_{g,HTM} &\leq 0 \\
\chi_{HTM} + E_{g,HTM} - \chi_P - E_{g,P} &\leq 0 \\
\chi_P - \chi_{ETM} &\leq 0
\end{aligned} \tag{6}$$

where Φ_F, Φ_B are the front and back contact workfunctions. For simplicity, we compute them via the flat-band approximation by equating the work functions to the Fermi energies at $x = 0, L$. Denoting the intrinsic Fermi energy of a material as E_i , we have the following nonlinear relationships

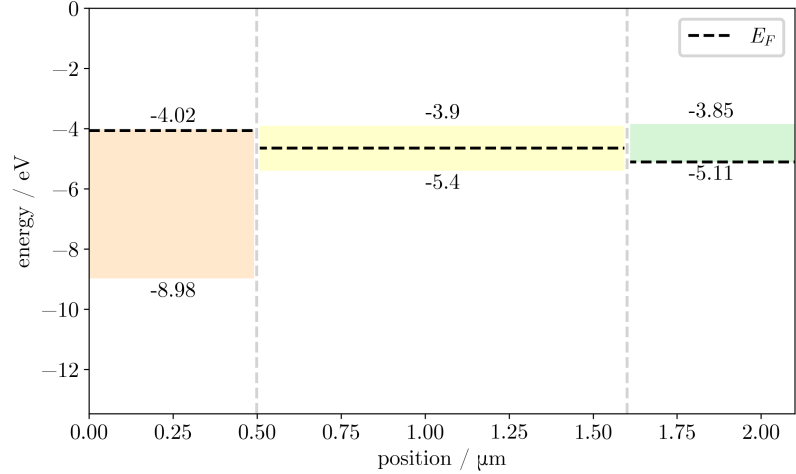
$$\begin{aligned}
\Phi_F &= E_{i,0} + k_B T \log \left(\frac{N_{d,0}}{n_{i,0}} \right) \\
\Phi_B &= E_{i,L} - k_B T \log \left(\frac{N_{a,L}}{n_{i,L}} \right).
\end{aligned} \tag{7}$$

For our nonlinear constrained optimization problem we select the Sequential Least Squares Programming (SLSQP) method [25]. SLSQP has been implemented in several open-source tools, including Optim [26], NLOpt [27], PyOpt [28] and Scipy [29]. For this work, we chose the last one. Starting from a randomly sampled initial design with 6.49% PCE, the algorithm terminates after only 306 PDE solves, arriving at an optimal point with PCE 21.62%. This is higher than that of all 200 randomly sampled designs, which amount to roughly 4000 PDE solves. This is illustrated in Figure 2a.

As mentioned above, in ∂PV it is possible to treat V as an additional variable to be differentiated through via the IFT as part of the intermediate parameters $\tilde{\mathbf{p}}$. At an optimal point, V will be selected as the corresponding MPP of the associated cell. Optimizing V and \mathbf{p} holistically rather than separately brings computational benefits, especially when two consecutive iterations have similar device parameters; in fact, we only need to sweep from these two close points in the $\tilde{\mathbf{p}}$ space rather than sweeping V twice from 0. In this case, when changing V of about 0.05 V (with all the other parameters varied accordingly), we obtain an overall savings in PDE solves of about 25%. The alternative procedure of optimizing V and \mathbf{p} separately is described in Appendix H.



(a)



(b)

Figure 2: Results of using SLSQP to optimize the ETL and HTL material properties of a PSC. a) Growth of the optimization objective compared with random search. The inset contains the PCE of 200 randomly sampled cells together with a kernel-estimated distribution, with the SLSQP optimal point (red) being superior to all samples while being more than 10 times more efficient in terms of PDE solves. Scattered points represent random samples. b) Isolated energy levels of the optimized PSC design.

4.2. Materials Discovery

The usefulness of gradients is not limited to direct optimization purposes. Here we present a simple demonstration of the potential of an adjoint model built within an AD framework. Unlike the previous example, here we need to compute the whole *IV* curve, therefore we only consider a subset of \mathbf{p} as optimization parameters. For simplicity, suppose we have an empirical *IV* curve of a simple p-n homojunction measured from a physical experiment. All material parameters are assumed to be known but for two: the band gap of the material making up the cell, E_g , and the hole mobility, μ_p . The idea is that given reasonable initial guesses of the parameters, one can recover the latent material property, assuming identifiability of *IV* curves, by minimizing a dissimilarity measure between the candidate and target *IV* curves, \hat{J} and J^* respectively. Formally, the problem to solve is to minimize over \mathbf{p}^* , the unknown parameters,

$$R(\hat{J}(\mathbf{p}^*), J^*) := \int_0^{\frac{\pi}{2}} [r^*(\theta) - \hat{r}(\theta, \mathbf{p}^*)]^2 d\theta \quad (8)$$

where $r^*(\theta)$ refers to the empirical *IV* curve reparameterized in polar coordinates, with the conventions that $\theta = 0$ corresponds to the positive y -axis and θ grows clockwise. The term \mathbf{p}^* has only the parameters to be discovered (two in this case). The gradient of \hat{r} with respect to \mathbf{p}^* are computed via AD. Eq. 8 corresponds to integrating the squared radial differences between the two curves over the first quadrant. The choice of parameterizing by θ comes from the observation that *IV* curves are monotonically decreasing from the point $(0, I_{sc})$ to $(V_{oc}, 0)$, and resemble arcs. *IV* curves are computed over $[0, V_{oc}]$, meaning that two curves generally have different support in V , causing discontinuities if we were to integrate differences only in the intersection. In contrast, the support of $[0, \pi/2]$ is always promised in polar coordinates. Meanwhile, the distance measure chosen avoids this issue, and additionally presents pleasant optimization properties, such as smoothness and symmetry, that play a crucial role in the success of this methodology. Note that in a practical implementation, quadratic interpolation and a discrete approximation of the integral are used.

SLSQP was once again used for this problem. The algorithm takes less than 10 function calls to arrive at the correct parameters of $E_g = 1.0$, $\log_{10} \mu_p = 2.20$ from initial values of 1.2 and 2.0 respectively. It must be stressed that while the empirical *IV* curve is generated through simulation

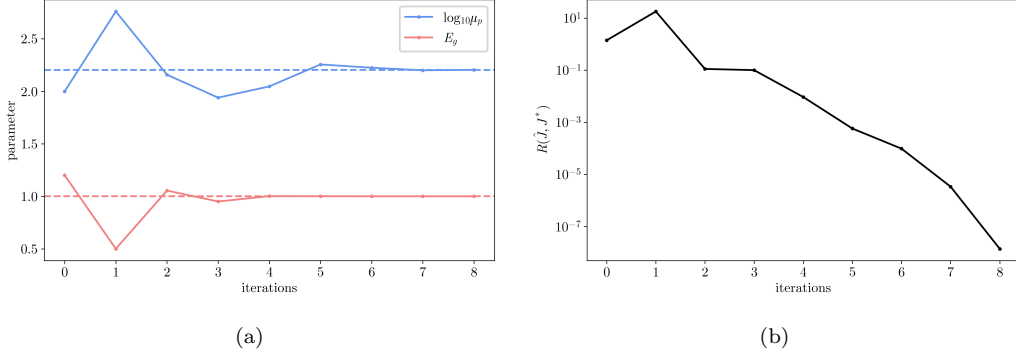


Figure 3: SLSQP results for minimizing the distance between a candidate IV curve and the empirical curve. In this minimal example, the process converges within less than 10 function calls. (a) Trajectory of E_g and $\log_{10} \mu_p$, the estimated latent parameters. (b) The objective over the descent process in log scale. Note it converges to zero rapidly.

for the sake of this example, in a meaningful application it would come from an experiment.

5. Conclusion

We have presented a composable, differentiable PV simulator that, while enabling new data-efficient optimization and materials discovery techniques, does not compromise on computational speed. Being built with sparse linear-algebra compatibility in mind, ∂PV has the potential to be easily extended to 2-dimensional or 3-dimensional modeling in the future. This promises more realistic and general modeling for developing novel structures. With JAX also rapidly growing in popularity, the ecosystem for working with ∂PV is likely to grow as well.

6. Acknowledgments

We thank Rachel Kurchin and Matthias auf Der Maur for helpful discussions. We also thank Arthur Reiner De Belen for writing an initial draft for the online documentation. This work was supported in part by a fellowship from Eni S.p.A. and the MIT Energy Initiative.

Constants			
Notation	Physical Quantity	Notation	Physical Quantity
ϵ_0	vacuum permittivity	q	elementary charge
k_B	Boltzmann constant	T	temperature
Material Parameters			
Notation	Physical Quantity	Notation	Physical Quantity
ϵ	relative permittivity	E_g	band gap
χ	electron affinity	N_c	density of states at the conduction band
N_v	density of states at the valence band	N_a	acceptor dopant density
N_d	donor dopant density	μ_n	electron mobility
μ_p	hole mobility	B	radiative recombination coefficient
C_n	electron Auger coefficient	C_p	hole Auger coefficient
E_t	trap energy level for SRH recombination	t_n	bulk electron lifetime
t_p	bulk hole lifetime	S_n	electron surface recombination velocity
S_p	hole surface recombination velocity		
Variables			
Notation	Physical Quantity	Notation	Physical Quantity
ϕ	electrostatic potential	ϕ_n	electron quasi-Fermi energy
ϕ_p	hole quasi-Fermi energy	n	electron density
p	hole density	J_n	electron current
J_p	hole current		

Table A.1: Notation for the physical quantities used in the model. In the model described in this work, the temperature is considered constant at 300K. Variables are physical quantities that must be solved for in the solar cell equations.

Appendix A. The Drift-Diffusion model

The DD method couples the continuity equations for electrons and holes with the Poisson equation. In the absence of a temperature gradient it reads as

$$\begin{aligned}
\epsilon_0 \vec{\nabla} \cdot (\epsilon \vec{\nabla} \phi) &= q(n - p + N_a - N_d) \\
\vec{\nabla} \cdot \vec{J}_n &= -q(G - R) \\
\vec{\nabla} \cdot \vec{J}_p &= q(G - R) \\
\vec{J}_n &= q\mu_n n \vec{\nabla} \phi_n \\
\vec{J}_p &= q\mu_p p \vec{\nabla} \phi_p
\end{aligned} \tag{A.1}$$

where R is the total recombination rate density, G is the electron-hole pair generation density, N_a (N_d) the acceptor (donor) density, ϵ the relative dielectric constant, $\mu_{n(p)}$ the electron (hole) mobility, q the electron charge, and $\phi_{n(p)}$ the electrochemical potential for electrons (holes). The electron (n) and hole (p) densities are given by

$$\begin{aligned}
n &= N_c \exp\left(\frac{\phi_n + \chi + q\phi}{k_B T}\right) \\
p &= N_v \exp\left(\frac{-\phi_p - \chi - E_g - q\phi}{k_B T}\right)
\end{aligned} \tag{A.2}$$

, where χ is the electron affinity, k_B the Boltzmann constant, and E_g the energy gap.

The radiative, Auger and Shockley-Read-Hall (SRH) recombination terms are readily expressed as a function of the electron/hole densities and the intrinsic carrier density $n_i = \sqrt{N_c N_v} \exp(\frac{E_g}{2k_B T})$:

$$\begin{aligned}
R_{radiative} &= B(np - n_i^2) \\
R_{Auger} &= (C_n n + C_p p)(np - n_i^2) \\
R_{SRH} &= \frac{np - n_i^2}{t_n \left(n + n_i \exp\left(\frac{E_t}{k_B T}\right) \right) + t_p \left(p + n_i \exp\left(-\frac{E_t}{k_B T}\right) \right)},
\end{aligned} \tag{A.3}$$

where E_t is the trap energy level, $C_{n(p)}$ the electron (hole) Auger coefficient, and $t_{n(p)}$ is the electron (hole) bulk lifetime.

Appendix B. Optics

The calculation of the generation density $G(x)$ requires an absorption model for the incoming phonon flux. To this end, we use the simple Beer–Lambert approximation

$$S(\lambda, x) = S_{\text{sun}}(\lambda) \exp \left(- \int_0^x \alpha(\lambda, x') dx' \right), \quad (\text{B.1})$$

where $S(\lambda, x)$ is the spectral irradiance of the incoming radiation at distance x and for wavelength λ . The direct band gap model is used to calculate the absorption coefficient as follows:

$$\alpha(\lambda, x) = \begin{cases} A \sqrt{\frac{hc}{\lambda} - E_g(x)} & \text{if } \frac{hc}{\lambda} \geq E_g(x) \\ 0 & \text{otherwise} \end{cases} \quad (\text{B.2})$$

The photon flux density is then given by

$$\varphi(x) = \int_0^\infty \frac{S(\lambda, x)}{hc/\lambda} d\lambda \quad (\text{B.3})$$

In order to integrate over the highly ragged solar spectrum, we employ a Gaussian quadrature scheme [30] which computes, in advance, a small number M of nodes $\tilde{\lambda}_i$ and their respective effective weights \tilde{I}_i which together approximate to great accuracy integrals of the form

$$\int_0^\infty S_{\text{sun}}(\lambda) f(\lambda) d\lambda \approx \sum_{i=1}^M \tilde{I}_i f(\tilde{\lambda}_i) \quad (\text{B.4})$$

The generation density can then be found by differentiating the photon flux, giving

$$G(x) = \sum_{i=1}^M \frac{\tilde{\lambda}_i \tilde{I}_i}{hc} \alpha(\tilde{\lambda}_i, x) \exp \left(- \int_0^x \alpha(\tilde{\lambda}_i, x') dx' \right) \quad (\text{B.5})$$

Appendix C. The boundary conditions

We consider unidimensional solar cells spanning the x axis from $x = 0$ to $x = L$. When the system is at equilibrium (no net flow of carriers), there is

no current, therefore the quasi-Fermi energies are constant across the system, and are set to zero : $\phi_n = \phi_p = 0$. Therefore we must solve only the Poisson equation, where we implement the common Dirichlet boundary conditions for Ohmic and Schottky contacts. For Ohmic contacts, depending on whether the contact at $x = 0, L$ is n -doped or p -doped we have:

$$\phi(x = 0, L) = \begin{cases} -\chi + k_B T \ln\left(\frac{N_d}{N_c}\right) & n\text{-doped} \\ -\chi - E_g - k_B T \ln\left(\frac{N_a}{N_v}\right) & p\text{-doped} \end{cases} \quad (\text{C.1})$$

Where the front and back contact workfunctions Φ_F, Φ_B are provided, we impose the Schottky boundary conditions:

$$\begin{aligned} \phi(0) &= -\Phi_F \\ \phi(L) &= -\Phi_B \end{aligned} \quad (\text{C.2})$$

When the system is out of equilibrium and we impose a bias voltage V :

$$\begin{aligned} \phi(0) &= \phi_{eq}(0) \\ \phi(L) &= \phi_{eq}(L) + V \\ J_n(0) &= qS_{n,0}(n(0) - n_{eq}(0)) \\ J_n(L) &= -qS_{n,L}(n(L) - n_{eq}(L)) \\ J_p(0) &= -qS_{p,0}(p(0) - p_{eq}(0)) \\ J_p(L) &= qS_{p,L}(p(L) - p_{eq}(L)) \end{aligned} \quad (\text{C.3})$$

where n_{eq}, p_{eq} are the equilibrium electron/hole densities, and $S_{n/p,0/L}$ are the surface recombination velocities at the $x = 0, L$ contacts for electrons/holes.

Appendix D. The Scharfetter–Gummel method

We solve the drift-diffusion model using finite differences. The system is now defined over a grid $x = x_i$ for $1 \leq i \leq N$, where a difference is made between material properties and variables defined over the “grid points” x_i and the “slabs” between consecutive $x_i \rightarrow x_{i+1}$ over which the current densities are defined and computed. Thus, material parameters and variables defined throughout the system are now vectors : $u(x) \rightarrow \{u(x_i)\}_{1 \leq i \leq N}$. For the discretization of the current, we use the Scharfetter-Gummel scheme over

the “slabs” [31], which defines trial functions for the current to evaluate the gradient of the currents that appears in the continuity equations, in order to ensure numerical convergence. In this work, we follow the discretization as outlined in SESAME [4], where the currents are defined as follows:

$$\begin{aligned}
\Psi_{n,i} &= q\phi_i + \chi_i + k_B T \ln(N_{c,i}) \\
\Psi_{p,i} &= q\phi_i + \chi_i + E_{g,i} - k_B T \ln(N_{v,i}) \\
J_n^{i \rightarrow i+1} &= -\frac{q\mu_{n,i}}{x_{i+1} - x_i} \frac{\Psi_{n,i+1} - \Psi_{n,i}}{\exp(-\frac{\Psi_{n,i+1}}{k_B T}) - \exp(-\frac{\Psi_{n,i}}{k_B T})} \left(\exp(\frac{\phi_{n,i+1}}{k_B T}) - \exp(\frac{\phi_{n,i}}{k_B T}) \right) \\
J_p^{i \rightarrow i+1} &= \frac{q\mu_{p,i}}{x_{i+1} - x_i} \frac{\Psi_{p,i+1} - \Psi_{p,i}}{\exp(-\frac{\Psi_{p,i+1}}{k_B T}) - \exp(-\frac{\Psi_{p,i}}{k_B T})} \left(\exp(-\frac{\phi_{p,i+1}}{k_B T}) - \exp(-\frac{\phi_{p,i}}{k_B T}) \right)
\end{aligned} \tag{D.1}$$

Therefore, the discretized gradient of the current is:

$$\begin{aligned}
\frac{dJ_n}{dx} \Big|_i &= \frac{J_n^{i \rightarrow i+1} - J_n^{i-1 \rightarrow i}}{\frac{x_{i+1} - x_{i-1}}{2}} \\
\frac{dJ_p}{dx} \Big|_i &= \frac{J_p^{i \rightarrow i+1} - J_p^{i-1 \rightarrow i}}{\frac{x_{i+1} - x_{i-1}}{2}}
\end{aligned} \tag{D.2}$$

Finally, the discretized Laplacian on the left side of the Poisson equation is simply (where the divergence is taken as a central derivative):

$$\frac{d(\epsilon \frac{d\phi}{dx})}{dx} \Big|_i = \frac{1}{\frac{x_{i+1} - x_{i-1}}{2}} \left(\frac{\epsilon_{i+1} + \epsilon_i}{2} \frac{\phi_{i+1} - \phi_i}{x_{i+1} - x_i} - \frac{\epsilon_i + \epsilon_{i-1}}{2} \frac{\phi_i - \phi_{i-1}}{x_i - x_{i-1}} \right) \tag{D.3}$$

Thus, the system of differential equations becomes an equation for the zeros of the F function of $3N$ variables $\{\phi_{n,i}, \phi_{p,i}, \phi_i\}_{1 \leq i \leq N} = \{u_i\}_{1 \leq i \leq 3N}$, $F : \mathbb{R}^{3N} \rightarrow \mathbb{R}^{3N}$, where 6 components of F are the discretized boundary conditions, and the other $3(N-2)$ are the discretized continuity and Poisson equations.

Appendix E. Linear solver

To accomodate possible future extensions to 2D and 3D modelling, ∂PV computes and stores the band-diagonal Jacobian in a standard compact format allowing only $O(N)$ memory. The linear solve is done via the Generalized Minimum Residual (GMRES) method [32], provided by JAX, which iteratively

finds a minimal-residual vector in a Krylov subspace for a large, sparse, and asymmetric system. An *ILU(0)* preconditioner [33] for band-diagonal matrices was developed to drastically improve the rate of convergence. The preconditioner is used to approximate the inverse of the Jacobian through performing an incomplete *LU* factorization in $O(N)$ time that preserves the nonzero structure of the Jacobian, which is then used to operate on vectors through the standard two-step forward and backward substitutions.

Appendix F. The modified Newton algorithm

To avoid stagnation arising from the traditional Newton algorithm, we employ an element-wise damping scheme [4] for the Newton step

$$\tilde{z}_j^{(i)} = \begin{cases} z_j^{(i)} & \text{if } -1 \leq z_j^{(i)} \leq 1 \\ \text{sgn}(z_j^{(i)}) \ln(1 + (e - 1) \cdot |z_j^{(i)}|) & \text{otherwise} \end{cases} \quad (\text{F.1})$$

where e refers to Euler's number. We speculate that this damping scheme works well because of the exponential nature of the drift-diffusion system. As an example, consider performing Newton–Raphson on the function $f(x) = e^x - 1$ with an initial guess $x_0 < 0$ to find its root, which is trivially zero. The unmodified Newton step at any x is given by

$$z = -\frac{e^x - 1}{e^x} = e^{-x} - 1 \quad (\text{F.2})$$

Supposing that x_0 is sufficiently far away from zero, the Newton step is then dominated by the term e^{-x_0} , which is exponential in the correct step $-x_0$. Using the unmodified Newton step would thus cause a huge overshoot, accompanied by numerical overflow issues. It intuitively makes sense to set a threshold on the step size, above which we take the log for a more accurate estimation of the correct step.

It is also interesting to consider the other case, where $x_0 > 0$ with x_0 sufficiently far away from zero. Here, z approaches -1 regardless of the distance from the root, which results in slow convergence. This is alleviated in ∂PV by an additional “acceleration” modification on top of the damping as follows

$$\delta \mathbf{u}^{(i)} = \tilde{\mathbf{z}}^{(i)} + \max\left\{\frac{\tilde{\mathbf{z}}^{(i)} \cdot \tilde{\mathbf{z}}^{(i-1)}}{|\tilde{\mathbf{z}}^{(i)}||\tilde{\mathbf{z}}^{(i-1)}|}, 0\right\} \cdot \delta \mathbf{u}^{(i-1)} \quad (\text{F.3})$$

which has the effect of “accumulating” previous steps when the new damped Newton step is sufficiently similar to the previous one. This effectively allows successive steps to grow quadratically when required.

To ensure convergence of Newton–Raphson, it is standard practice to use the solution at a bias voltage V_i as the initial guess for the next step V_{i+1} . ∂PV takes this one step further by performing forward extrapolation, using the solutions for V_i and V_{i-1} to compute a significantly more accurate guess of the solution for V_{i+1} . Through fitting a quadratic curve, for each grid point, through the three most recent solutions at equally spaced voltages, we obtain

$$\tilde{\phi}_j^{i+1} = 3\phi_j^i - 3\phi_j^{i-1} + \phi_j^{i-2} \quad (\text{F.4})$$

where $\tilde{\phi}_j^{i+1}$ is the initial guess for the electrostatic potential at grid position j for V_{i+1} . This simple trick was found to notably improve both convergence behavior and computation time.

Appendix G. Implicit Function Theorem

Essentially, we note that the solution to the drift-diffusion system implicitly depends on $\tilde{\mathbf{p}}$ itself, e.g. $\mathbf{f}(\mathbf{u}^*(\tilde{\mathbf{p}}), \tilde{\mathbf{p}}) = 0$, where \mathbf{u}^* is the solution of Eq. 1. Hence the total derivative of \mathbf{f} with respect to $\tilde{\mathbf{p}}$ is given by

$$\mathbf{f}_u \mathbf{u}_{\tilde{\mathbf{p}}}^* + \mathbf{f}_{\tilde{\mathbf{p}}} = 0, \quad (\text{G.1})$$

all the quantities being computed at \mathbf{u}^* . Equation G.1 leads to

$$\mathbf{u}_{\tilde{\mathbf{p}}}^* = -\mathbf{f}_u^{-1} \mathbf{f}_{\tilde{\mathbf{p}}}; \quad (\text{G.2})$$

which provides a much simpler way to obtain the gradients. Note that \mathbf{f}_u^{-1} is just the Jacobian used in the computation of the Newton step, and is thus available for free. Meanwhile, $\mathbf{f}_{\tilde{\mathbf{p}}}$, which follows directly from the drift-diffusion equations, can be obtained easily with AD. While we have bypassed the need for differentiating through iterative solvers, there are still M linear systems to solve in this approach. In fact, a linear system should be solved for each column of $\mathbf{f}_{\tilde{\mathbf{p}}}$. These problems can be solved by either using a direct method, while reusing the LU factorization, or with an iterative approach, commonly based on block Krylov subspaces. However, here the problem is simplified by taking advantage of *reverse-mode* AD. In fact, this method is preferred over forward-mode AD for wide Jacobians. Our case

is the limiting one where the Jacobian has only one row, i.e. the gradient $dI/d\tilde{\mathbf{p}}$. In reverse-mode AD, programs can be seen as the composition of vector-Jacobian-products (VJP), i.e. $\mathbf{v}^T \mathbf{J}$, or, equivalently, $\mathbf{J}^T \mathbf{v}$, where \mathbf{v} is a generic vector. In relation to Eq. G.3, we seek an expression for $\mathbf{v}^T \mathbf{u}_\mathbf{p}^*$. To this end, we simply multiply both sides of Eq. G.3 by \mathbf{v}^T

$$\mathbf{v}^T \mathbf{u}_\mathbf{p}^* = -\mathbf{v}^T \mathbf{f}_\mathbf{u}^{-1} \mathbf{f}_{\tilde{\mathbf{p}}} = \lambda^T \mathbf{f}_{\tilde{\mathbf{p}}}, \quad (\text{G.3})$$

where λ^T is the solution of the linear system

$$\mathbf{f}_\mathbf{u}^T(\mathbf{u}^*) \lambda = -\mathbf{v}; \quad (\text{G.4})$$

We note that Eq. G.4 represents the adjoint of the linearized original problem (Eq. 2) at $\mathbf{u} = \mathbf{u}^*$ [22]. Because reverse AD involves the transposed Jacobian (and hence solving a transpose of the original linear system), reverse-mode AD is also known as an “adjoint” method when it is implemented by hand [34]. In ∂PV we simply provide the VJP from Eq. G.3 and JAX will then compose it with other JVPs, e.g. those arising from Eq. H.2, to perform end-to-end reverse AD.

Appendix H. An alternative optimization approach

∂PV also provides an optimization approach where V and p are optimized separately. In this case, one simulation yields a sequence of k points on the IV curve, $(V_1, I_1) \dots (V_k, I_k)$ and then P_{MPP} usually taken as the maximum $V_i I_i$ over this discrete set. In ∂PV , to ensure differentiability, we interpolate $P(V)$ with a quadratic spline, then analytically maximize to compute the MPP. The PCE $\eta = Q(\mathbf{I})$ is a function of the k points computed on the IV curve, where $\mathbf{I} = \text{vec}(I_1, \dots, I_k)$ is the vectorization of the current $I(\mathbf{u}, \tilde{\mathbf{p}})$ at different voltages. Q denotes the operation of approximating $P(V)$ with a quadratic spline, then maximizing analytically. The bias voltages are evenly spaced with a step size of 0.05 V, so it is not necessary to consider them as explicit variables. The gradient of the efficiency reads

$$\frac{d\eta}{d\mathbf{p}} = Q_{\mathbf{I}} \frac{d\mathbf{I}}{d\mathbf{p}} = \sum_{j=1}^k Q_{I_j} \frac{dI_j}{d\mathbf{p}}, \quad (\text{H.1})$$

where \mathbf{p} includes only the input material parameters. The derivative $Q_{\mathbf{I}}$ is obtained with AD to link the gradients for each individual PDE solution to

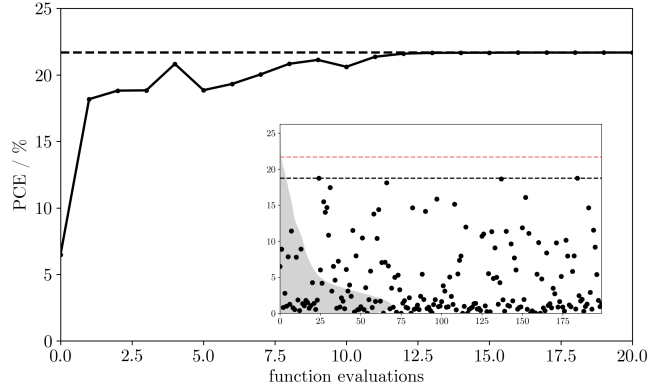


Figure H.4: The PCE versus the number of iterations of the SLSQP algorithm. The optimized structure has a PCE of about 21.62%. In the inset, the PCEs for randomly chosen configurations are shown.

the PCE. Meanwhile, upon further analysis we have

$$\frac{dI}{d\tilde{\mathbf{p}}} = I_{\mathbf{u}} \mathbf{u}_{\tilde{\mathbf{p}}} + I_{\tilde{\mathbf{p}}}, \quad (\text{H.2})$$

where, for simplicity, we dropped the subscript j . From now on, we can use the IFT, as detailed in Appendix G.

In ∂PV , to ensure smoothly varying results, we use a quadratic spline to construct a once-differentiable interpolation $\tilde{P}(V)$ of the power-voltage curve given the discrete points evaluated, which is a sequence of $k - 1$ quadratic functions $\tilde{P}_1 \dots \tilde{P}_{k-1}$ with the following constraints

$$\begin{cases} \tilde{P}_i(V_i) = V_i I_i & \text{for } 1 \leq i \leq k - 1 \\ \tilde{P}_i(V_{i+1}) = V_{i+1} I_{i+1} & \text{for } 1 \leq i \leq k - 1 \\ \tilde{P}'_i(V_{i+1}) = \tilde{P}'_{i+1}(V_{i+1}) & \text{for } 1 \leq i \leq k - 2 \\ \tilde{P}'_1(x) \equiv 0 & \end{cases} \quad (\text{H.3})$$

then calculate the MPP analytically by maximizing each \tilde{P}_i over their respective domains. The benefits are two-fold: aside from continuity, this also allows larger voltage steps to be taken while preserving a good estimate of the MPP, and thus the PCE, via spline interpolation. This means that IV curves can typically be computed to a satisfactory degree of precision and accuracy with only around 20 voltage steps. We use SLSQP algorithm for

nonlinear optimization. The final structure has the same PCE as that identified using V as an optimization variable, but with a smoother convergence, shown Fig. H.4. However, the overall number of PDE solves is 400, versus 306 needed for the holistic approach. ∂PV provides both optimization techniques.

References

- [1] D. A. Clugston, P. A. Basore, Pcl1d version 5: 32-bit solar cell modeling on personal computers, in: Conference Record of the Twenty Sixth IEEE Photovoltaic Specialists Conference - 1997, 1997, pp. 207–210. doi: [10.1109/PVSC.1997.654065](https://doi.org/10.1109/PVSC.1997.654065).
- [2] M. Burgelman, P. Nollet, S. Degrave, Modelling polycrystalline semiconductor solar cells, *Thin Solid Films* 361-362 (2000) 527–532. doi:[https://doi.org/10.1016/S0040-6090\(99\)00825-1](https://doi.org/10.1016/S0040-6090(99)00825-1). URL <https://www.sciencedirect.com/science/article/pii/S0040609099008251>
- [3] Y. Liu, D. Heinzel, A. Rockett, A new solar cell simulator: Wxamps, Conference Record of the IEEE Photovoltaic Specialists Conference (2011) 002753–002756doi: [10.1109/PVSC.2011.6186517](https://doi.org/10.1109/PVSC.2011.6186517).
- [4] B. Gaury, Y. Sun, P. Bermel, P. Haney, Sesame: A numerical simulation tool for polycrystalline photovoltaics, in: 2018 IEEE 7th World Conference on Photovoltaic Energy Conversion (WCPEC) (A Joint Conference of 45th IEEE PVSC, 28th PVSEC 34th EU PVSEC), 2018, pp. 1882–1885. doi: [10.1109/PVSC.2018.8548291](https://doi.org/10.1109/PVSC.2018.8548291).
- [5] S. Kumazawa, S. Shibusawa, T. Nishio, T. Aramoto, H. Higuchi, T. Arita, A. Hanafusa, K. Omura, M. Murozono, H. Takakura, 15.1highly efficient thin film cdscdte solar cell, *Solar Energy Materials and Solar Cells* 49 (1) (1997) 205–212. doi:[https://doi.org/10.1016/S0927-0248\(97\)00196-7](https://doi.org/10.1016/S0927-0248(97)00196-7). URL <https://www.sciencedirect.com/science/article/pii/S0927024897001967>
- [6] N.-G. Park, Perovskite solar cells: an emerging photovoltaic technology, *Materials Today* 18 (2) (2015) 65–72. doi:<https://doi.org/10.1016/j.mattod.2014.07.007>.

URL <https://www.sciencedirect.com/science/article/pii/S1369702114002570>

- [7] J. S. Yun, A. Ho-Baillie, S. Huang, S. H. Woo, Y. Heo, J. Seidel, F. Huang, Y.-B. Cheng, M. A. Green, Benefit of grain boundaries in organic–inorganic halide planar perovskite solar cells, *The Journal of Physical Chemistry Letters* 6 (5) (2015) 875–880, pMID: 26262666. [arXiv:https://doi.org/10.1021/acs.jpclett.5b00182](https://doi.org/10.1021/acs.jpclett.5b00182), doi:10.1021/acs.jpclett.5b00182.
URL <https://doi.org/10.1021/acs.jpclett.5b00182>
- [8] J. M. Ball, A. Petrozza, Defects in perovskite-halides and their effects in solar cells, *Nature Energy* 1 (11) (2016) 16149. doi:10.1038/nenergy.2016.149.
URL <https://doi.org/10.1038/nenergy.2016.149>
- [9] J. Bradbury, R. Frostig, P. Hawkins, M. J. Johnson, C. Leary, D. Maclaurin, G. Necula, A. Paszke, J. VanderPlas, S. Wanderman-Milne, Q. Zhang, JAX: composable transformations of Python+NumPy programs (2018).
URL <http://github.com/google/jax>
- [10] A. G. Baydin, B. A. Pearlmutter, A. A. Radul, J. M. Siskind, Automatic differentiation in machine learning: a survey, *Journal of machine learning research* 18 (2018).
- [11] D. Maclaurin, D. Duvenaud, R. P. Adams, Autograd: Effortless gradients in numpy, in: ICML 2015 AutoML Workshop, Vol. 238, 2015, p. 5.
- [12] C. Rackauckas, A. Edelman, K. Fischer, M. Innes, E. Saba, V. B. Shah, W. Tebbutt, Generalized physics-informed learning through language-wide differentiable programming., in: AAAI Spring Symposium: MLPS, 2020.
- [13] S. Schoenholz, E. D. Cubuk, Jax md: a framework for differentiable physics, *Advances in Neural Information Processing Systems* 33 (2020).
- [14] P. Eastman, J. Swails, J. D. Chodera, R. T. McGibbon, Y. Zhao, K. A. Beauchamp, L.-P. Wang, A. C. Simmonett, M. P. Harrigan, C. D.

Stern, et al., Openmm 7: Rapid development of high performance algorithms for molecular dynamics, *PLoS computational biology* 13 (7) (2017) e1005659.

- [15] D. Kochkov, J. A. Smith, A. Alieva, Q. Wang, M. P. Brenner, S. Hoyer, Machine learning accelerated computational fluid dynamics, arXiv preprint arXiv:2102.01010 (2021).
- [16] C. P. Goodrich, E. M. King, S. S. Schoenholz, E. D. Cubuk, M. P. Brenner, Designing self-assembling kinetics with differentiable statistical physics models, *Proceedings of the National Academy of Sciences* 118 (10) (2021).
- [17] A. F. Oskooi, D. Roundy, M. Ibanescu, P. Bermel, J. D. Joannopoulos, S. G. Johnson, Meep: A flexible free-software package for electromagnetic simulations by the fdtd method, *Computer Physics Communications* 181 (3) (2010) 687–702.
- [18] Y. Hu, L. Anderson, T.-M. Li, Q. Sun, N. Carr, J. Ragan-Kelley, F. Durand, Difftaichi: Differentiable programming for physical simulation, arXiv preprint arXiv:1910.00935 (2019).
- [19] J. A. Nelson, *The physics of solar cells*, World Scientific Publishing Company, 2003.
- [20] A. GalÁjtai, The theory of newton's method, *Journal of Computational and Applied Mathematics* 124 (1) (2000) 25–44, numerical Analysis 2000. Vol. IV: Optimization and Nonlinear Equations. doi:[https://doi.org/10.1016/S0377-0427\(00\)00435-0](https://doi.org/10.1016/S0377-0427(00)00435-0).
URL <https://www.sciencedirect.com/science/article/pii/S0377042700004350>
- [21] S. G. Krantz, H. R. Parks, *The implicit function theorem: history, theory, and applications*, Springer Science & Business Media, 2012.
- [22] C. C. Margossian, A review of automatic differentiation and its efficient implementation, *Wiley interdisciplinary reviews: data mining and knowledge discovery* 9 (4) (2019) e1305.
- [23] C. R. Harris, K. J. Millman, S. J. van der Walt, R. Gommers, P. Virtanen, D. Cournapeau, E. Wieser, J. Taylor, S. Berg, N. J. Smith,

R. Kern, M. Picus, S. Hoyer, M. H. van Kerkwijk, M. Brett, A. Haldane, J. F. del R’io, M. Wiebe, P. Peterson, P. G’erard-Marchant, K. Sheppard, T. Reddy, W. Weckesser, H. Abbasi, C. Gohlke, T. E. Oliphant, Array programming with NumPy, *Nature* 585 (7825) (2020) 357–362. doi:10.1038/s41586-020-2649-2.
 URL <https://doi.org/10.1038/s41586-020-2649-2>

[24] A. A. Baloch, S. P. Aly, M. I. Hossain, F. El-Mellouhi, N. Tabet, F. H. Alharbi, Full space device optimization for solar cells, *Scientific reports* 7 (1) (2017) 1–14.

[25] D. Kraft, K. Schnepper, Slsqp—a nonlinear programming method with quadratic programming subproblems, DLR, Oberpfaffenhofen 545 (1989).

[26] P. K. Mogensen, A. N. Riseth, Optim: A mathematical optimization package for julia, *Journal of Open Source Software* 3 (24) (2018).

[27] S. G. Johnson, The nlopt nonlinear-optimization package (2014).

[28] R. E. Perez, P. W. Jansen, J. R. Martins, pyopt: a python-based object-oriented framework for nonlinear constrained optimization, *Structural and Multidisciplinary Optimization* 45 (1) (2012) 101–118.

[29] P. Virtanen, R. Gommers, T. E. Oliphant, M. Haberland, T. Reddy, D. Cournapeau, E. Burovski, P. Peterson, W. Weckesser, J. Bright, et al., Scipy 1.0: fundamental algorithms for scientific computing in python, *Nature methods* 17 (3) (2020) 261–272.

[30] S. G. Johnson, Accurate solar-power integration: Solar-weighted gaussian quadrature (2019). arXiv:1912.06870.

[31] H. K. Gummel, A self-consistent iterative scheme for one-dimensional steady state transistor calculations, *IEEE Transactions on Electron Devices* 11 (10) (1964) 455–465. doi:10.1109/T-ED.1964.15364.

[32] Y. Saad, M. H. Schultz, Gmres: A generalized minimal residual algorithm for solving nonsymmetric linear systems, *SIAM Journal on scientific and statistical computing* 7 (3) (1986) 856–869.

- [33] Y. Saad, Ilut: A dual threshold incomplete lu factorization, *Numerical linear algebra with applications* 1 (4) (1994) 387–402.
- [34] G. Strang, Computational science and engineering, no. Sirsi) i9780961408817, 2007.